Interstitial defects in the van der Waals gap of Bi_2Se_3

Interstitial defects in the Van der Waals gap of Bi_2Se_3

Authors

Carolien Callaert[a]*, Marnik Bercx[a], Dirk Lamoen[a] and Joke Hadermann[a]

[a]EMAT, Department of Physics, University of Antwerp, Groenenborgerlaan 171, 2020 Antwerp, Belgium

Correspondence email: Carolien.Callaert@uantwerpen.be

Funding information University of Antwerp (grant No. 31445).

Synopsis STEM and EDX uncovered interstitial defects with mainly Bi character in Bi_2Se_3. This is supported by PEDT and DFT calculations. The electron beam used during the STEM experiment induced atomic displacements across and along the Van der Waals gap, though climbing-image NEB calculations show that some paths could also occur spontaneously at room temperature.

Abstract Bi_2Se_3 is a thermoelectric material and a topological insulator. It is slightly conducting in its bulk due to the presence of defects, and controlling the defects allows fine-tuning the different physical properties. However, studies of the defects in this material are often contradicting or inconclusive. In this paper, the defect structure of Bi_2Se_3 is studied with a combination of techniques: high resolution-scanning transmission electron microscopy (HR-STEM), high resolution-energy dispersive X-ray (HR-EDX) spectroscopy, precession electron diffraction tomography (PEDT), X-ray diffraction (XRD) and first-principles calculations using density-functional theory (DFT). Based on these results, not only the observed defects are discussed, but also the discrepancies in results or possibilities across the techniques. STEM and EDX revealed interstitial defects with mainly Bi character in an octahedral coordination in the Van der Waals gap, independent of the applied sample preparation method (focused ion beam milling or cryo-crushing). The inherent character of these defects is supported by their observation in the structure refinement of the EDT data. Moreover, the occupancy probability of the defects determined by EDT is inversely proportional with their corresponding DFT calculated formation energies. STEM also showed the migration of some atoms across and along the Van der Waals gap. The kinetic barriers calculated using DFT suggest that some paths are possible at room temperature, while others are most likely beam-induced.

Keywords: Bi_2Se_3; defect; TEM; DFT; EDT

1. Introduction

Bi_2Se_3 is both a thermoelectric material (Sun *et al.*, 2015) and topological insulator, i.e. a bulk insulating material with conducting surface states. Nevertheless, Bi_2Se_3 slightly conducts in its bulk

due to the presence of defects (Xia *et al.*, 2009; Hor *et al.*, 2009). Recently, topological insulators gained a lot of interest owing to their special physical properties and potential for applications like high speed electronics, because of an absence in backscattering for non-magnetic defects (Roushan *et al.*, 2009). Compared to other materials like Bi_2Te_3, Bi_2Se_3 has a larger bandgap of 0.3 eV (Xia *et al.*, 2009; Zhang *et al.*, 2009), which opens the door to spintronic applications at room temperature, such as memory devices. For example, recently Han *et al*. (Han *et al.*, 2017) observed a high spin-orbit torque efficiency on the magnetic layer CoTb by Bi_2Se_3. Bi_2Se_3 is also an ideal study sample and application-friendly due to its robust and simple surface states where the Dirac point lies inside the band gap (Xia *et al.*, 2009).

Defects influence the physical material properties, e.g. electrical (Tumelero *et al.*, 2016; Ramachandran *et al.*, 2017), optical (Ramachandran *et al.*, 2017), mechanical (Ramachandran *et al.*, 2017) and transport (Dai *et al.*, 2016; Wu *et al.*, 2016) properties. They also determine the carrier concentration (Ando, 2013) and can modify the band structure by shifting the Dirac point energy and Fermi energy (Dai *et al.*, 2016; Mann *et al.*, 2013). The Fermi level affects a.o. whether the bulk character is insulating or conducting. To achieve the ideal properties for a specific application, the native defects need to be optimized (Zhu *et al.*, 2016). For example, the thermoelectric performance depends a.o. on the Seebeck coefficient, the electrical conductivity and the carrier thermal conductivity. These parameters are influenced by the carrier concentration, which in turn depends on the amount and the character of the defects. Note that extrinsic doping can influence the formation energy of these defects, thus increasing or decreasing their chance of existence and consequently affecting the carrier concentration (Zhu *et al.*, 2016).

Not only the static point defects, but also the movement of point defects is important. For example, Bi_2Se_3 shows potential for Li-ion batteries (Ali *et al.*, 2013; Xu *et al.*, 2013), and Bi_2Se_3 integrated with carbon has already been proven to be a high-performance sodium-ion battery anode material (Xie *et al.*, 2018). Related topological insulators also already have applications in phase change devices. The phase transition is induced by temperature, laser or electric field, necessitating the study of the movement of defects as these can be the first step towards the transition. For example, the switching energy decreased for a structure consisting of alternating GeTe (normal insulator) and Sb_2Te_3 (topological insulator) layers, a material designed for interfacial phase-change memory (IPCM) devices (Tominaga, 2018; Tominaga *et al.*, 2011; Simpson *et al.*, 2011). Furthermore, Bi_2Te_3 nanowires are promising for phase-change random access memory (PRAM) applications (Han *et al.*, 2011).

The basic structure of Bi_2Se_3 consists of quintuple layers (QLs), Se1-Bi-Se2-Bi-Se1, where the QLs are weakly bound by Van der Waals (VdW) interactions (Fig. 1a) (Mishra *et al.*, 1997; Pérez Vicente *et al.*, 1999). However, different kinds of native defects are observed or theoretically predicted for Bi_2Se_3: Se and Bi vacancies (Dai *et al.*, 2016; Scanlon *et al.*, 2012; Unzueta *et al.*, 2016; Devidas *et*

al., 2014; Alpichshev *et al.*, 2012; Mann *et al.*, 2013; West *et al.*, 2012; Wang *et al.*, 2013; Xue *et al.*, 2013), substituted atoms (Dai *et al.*, 2016; Scanlon *et al.*, 2012; Mann *et al.*, 2013; West *et al.*, 2012; Wang *et al.*, 2013; Xue *et al.*, 2013; Urazhdin *et al.*, 2002; Huang *et al.*, 2012), interstitial Se atoms (Dai *et al.*, 2016), interstitial Bi atoms (Tumelero *et al.*, 2016; Jia *et al.*, 2014; Urazhdin *et al.*, 2004) and Bi_2 layers in the VdW gap (Huang *et al.*, 2012) (Fig. 1). Different settings, for example growth kinetics (e.g. fast/slow cooling) (Dai *et al.*, 2016), the Bi/Se ratio (Dai *et al.*, 2016; Jia *et al.*, 2014; Zhu *et al.*, 2016), extrinsic doping (Zhu *et al.*, 2016), deformation after synthesis (Zhu *et al.*, 2016), and annealing (Zhu *et al.*, 2016), lead to different defect concentrations. Se substituted at the Bi sites and Bi vacancies have so far only been found with theoretical calculations for Se-rich samples (Xue *et al.*, 2013; West *et al.*, 2012; Scanlon *et al.*, 2012). For Bi_2Se_3, Se vacancies V_{Se}, especially on the outer Se layers, and Bi substituted at the Se positions Bi_{Se}, are the most commonly accepted defects (Dai *et al.*, 2016; Mann *et al.*, 2013; Scanlon *et al.*, 2012; Unzueta *et al.*, 2016; Devidas *et al.*, 2014; West *et al.*, 2012; Wang *et al.*, 2013; Xue *et al.*, 2013; Urazhdin *et al.*, 2002). In theory, native and intrinsic point defects differ: intrinsic point defects are point defects in stoichiometric materials, native point defects in non-stoichiometric materials. In practice, however, people are less strict with these terms (Zhu *et al.*, 2016), and Se deficiency can occur in Bi_2Se_3 synthesized using stoichiometric amounts because Se is volatile (Hu *et al.*, 2014), making the final Bi/Se ratio unknown unless specifically measured.

Several examples in the literature indicate the existence of Se and Bi interstitials: Dai *et al*. (Dai *et al.*, 2016) suggested the presence of Se interstitials (Fig. 1c) in the VdW gap based on their high resolution scanning tunnelling microscopy (HR STM) observations combined with first-principles simulations. However, others (Mann *et al.*, 2013; Hor *et al.*, 2009; Alpichshev *et al.*, 2012) previously proposed Se vacancies based on analogous observations. Despite their thorough argumentation, the Se interstitial atoms were not unambiguously determined. Urazhdin *et al*. (Urazhdin *et al.*, 2004) mentioned Bi interstitial defects in the VdW gap observed with scanning tunnelling microscopy and spectroscopy (STM-STS). However, interpretation of these data is not straightforward, especially without simulations, as follows from the work of Dai *et al*. (Dai *et al.*, 2016). Jia *et al*. (Jia *et al.*, 2014) used indirect observations (increase of the cell parameters and a shift on the diffraction peak (015)) to suggest the presence of Bi interstitial defects for a 2:1.5 Bi:Se ratio prepared sample. Finally, Tumelero *et al*. (Tumelero *et al.*, 2016) found two stable Bi interstitial sites in the VdW gap using theoretical calculations: Bi in an octahedral coordination, Bi_{oct}, and in a tetrahedral coordination, Bi_{tetra} (Fig. 1c). They optimized the lattice parameters of the structures with defects and determined that Bi_{oct} had a lower formation energy than Bi_{tetra}. In fact, Bi_{oct} possessed the lowest formation energy among all defects for a Bi-rich sample and lowest or second lowest for a Se-rich sample, which indicates that its existence is plausible.

Although these examples from the literature suggest the existence of Bi and Se interstitial defects, clear and direct experimental evidence is still lacking. In this paper, we show the existence of interstitial defects inside the VdW gap using a combination of state-of-the-art techniques: scanning transmission electron microscopy (HR-STEM) using an aberration corrected TEM, energy dispersive X-ray (HR-EDX) spectroscopy using a four-detector Super-X configuration and precession electron diffraction tomography (PEDT). We compare our experimental results with first-principles calculations using density functional theory (DFT) to study the formation energy of the defects and their movement across and along the VdW gap. We also discuss our attempts at structure characterization with X-ray powder diffraction (PXRD) and single crystal X-ray diffraction (SCXRD). We show that for this specific case, PEDT with dynamical refinement seems the most reliable method to investigate the occurrence of interstitial defects.

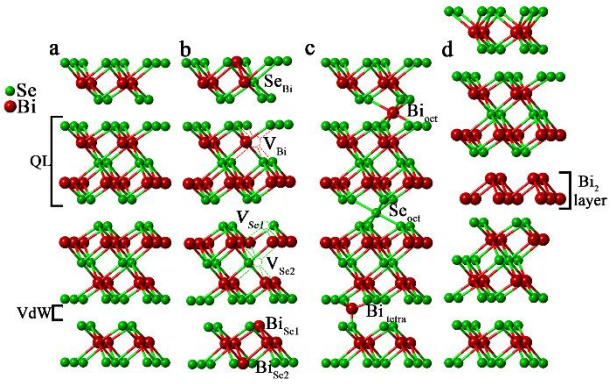

Figure 1 (a) Basic structure (Pérez Vicente *et al.*, 1999) of Bi_2Se_3, consisting of quintuple layers (QLs), Se1-Bi-Se2-Bi-Se1, with Van der Waals (VdW) interactions between the QLs. (b) Visualisation of the Se vacancies in the outer layers of the QL (V_{Se1}) and central Se layer (V_{Se2}), Bi vacancies (V_{Bi}), the substituted defects where Bi is substituted in the inner and outer layers of the QL (respectively Bi_{Se2} and Bi_{Se1}) and Se on the Bi sites (Se_{Bi}). (c) Interstitial Bi defects in the Van der Waals gap in the octahedral (Bi_{oct}) and tetrahedral coordination (Bi_{tetra}) and interstitial Se in an octahedral coordination. (d) Bi_2 layer modelled from the HAADF-STEM images of Huang *et al*. Green spheres are Se; red spheres are Bi. The corresponding references can be found in the main text.

2. Methodolology

2.1. Bulk sample preparation

The single-crystal bulk material of Bi_2Se_3 was prepared by melting stoichiometric amounts of Bi and Se in an evacuated sealed silica tube at 800 °C for 10h, cooling down to 670 °C for 2 days, and annealing at 670 °C for 5 days. Afterwards, we determined the Bi/Se ratio as 40.6(1.8)/59.4(1.8) using energy dispersive X-ray analysis (EDX) on a scanning electron microscope (SEM).

2.2. TEM

Transmission electron microscopy (TEM) samples were made with either focused ion beam (FIB) milling or with cryo-crushing combined with ultra-sonic bathing in ethanol. The cryo-crushing was performed by crushing the sample at liquid nitrogen temperature, and putting the crushed material in a glass tube with ethanol in an ultrasonic bath for approximately five minutes. Next, the solution was placed on a TEM grid. For the FIB sample, a Cu support was used and the top surface layer of the FIB lamella was protected by a carbon layer, followed by a platinum layer deposited with the electron beam and the ion beam, starting with the least invasive technique. Table 1 shows the thinning settings of the sample.

The STEM and EDX data were acquired on aberration-corrected Thermo Fisher Titan transmission electron microscopes operating at 300kV with an ultimate resolution of 0.8 Å. The EDX data is obtained with a Super-X four detector system. Calculated STEM images were made with QSTEM (Koch, 2002).

Table 1 Settings of the five step thinning process of the FIB lamella.

Step	High tension [kV]	Current [nA]	Angles [°]
1	30	0.79	51-53
2	30	0.23	51-53
3	30	0.08	51-53
4	8	0.066	50-54
5	2	0.023	48-56

Precession electron diffraction tomography (PEDT) data of the cryo-crushed TEM sample was acquired on a Thermo Fisher Tecnai G2 electron microscope at 200kV, using a CCD camera (2048x2048 px) and equipped with the ASTAR system from Nanomegas. Every 1° a precessed selected area electron diffraction pattern was taken from -21° to 76° (98 images) using a precession angle of 1° to minimize dynamical effects, and by tilting over the goniometer axis. The crystal had a random orientation at the start of the tilt series.

The program PETS (Palatinus, 2011) (Process Electron Tilt Series) was used to find the reflections, refine the orientation matrix, perform the cluster analysis and integrate the diffracted intensities. Next, the cluster reciprocal space was indexed using Jana2006 (Petrícek *et al.*, 2014), software which we also used to perform the structure refinement. The model for the kinematical refinement was the basic quintuple layer structure without defects. Afterwards, a dynamical refinement was performed, as implemented in the module Dyngo (refinement parameters: $R_{sg} = 0.4$, $g_{max} = 2$, 128 integration steps)

(Palatinus, Petříček *et al.*, 2015; Palatinus *et al.*, 2013; Palatinus, Corrêa *et al.*, 2015). An optimization of the orientation of each pattern was performed, and the frames with a tilt angle deviation higher than 0.5° were removed (9 frames). The refined parameters are the scale factors of the 89 frames, the occupancies, the positional parameters and the isotropic displacement parameters for all atoms, with some restrictions which are discussed in section 3.2. The cell parameters were updated to those determined from the PXRD data, which provides more accurate values, as the exact magnification of electron diffraction patterns can be anisotropic due to microscope aberrations and the total magnification can vary slightly during the series due to voltage instabilities and slight differences in sample height.

2.3. XRD

Powder X-ray diffraction (PXRD) data was acquired on a Huber G670 diffractometer, using Cu-K_α radiation (λ = 1.54059 Å). Lebail and Rietveld refinement were performed in Jana2006 (Petrícek *et al.*, 2014). Pseudo-Voigt functions consisting of the Gaussian parameters U, V, and W and the Lorentzian parameters X and Y, combined with an asymmetric correction by divergence (Finger *et al.*, 1994) were used to fit the PXRD data. Anisotropic strain broadening using the tensor method was applied. Ten Legendre Polynomials fit the background and a shift correction was introduced. The preferred orientation was corrected in the March Dollase approach (March, 1932; Dollase, 1986; Zolotoyabko, 2009). To reduce deformation due to mechanical stress, two PXRD sample preparation methods were performed: cryo-crushing and ultrasonic bathing in ethanol. For the latter, Bi_2Se_3 was submerged in ethanol and placed in an ultrasonic bath. The broken off Bi_2Se_3 fragments were collected five times after 10 minutes each in the ultrasonic bath and deposited on the holder. With each cycle, the ethanol was refilled. The procedure was paused every 5 minutes to regulate the water temperature of the ultrasonic bath.

2.4. DFT

First-principles calculations were carried out using density functional theory (DFT), encoded in the Vienna Ab initio Simulation Package (VASP) (Kresse & Hafner, 1993, 1994; Kresse & Furthmüller, 1996*a*,*b*). The generalized-gradient approximation of Perdew-Burke-Ernzerhof (PBE) (Perdew *et al.*, 1996, 1997) was used for the exchange and correlation energy. The Projector-Augmented Wave (PAW) method (Kresse & Joubert, 1999; Blöchl, 1994) was applied to describe the interactions between the ionic cores and the valence orbitals. $5d^{10}$ $6s^2$ $6p^3$ are the valence electrons for Bi and $4s^2$ $4p^4$ for Se. The VdW interaction was included using the optB86b-VdW density functional in VASP (Klimeš *et al.*, 2010, 2011). A plane wave basis with cut-off energy of 400 eV was utilized to describe the atoms in a 3x3x1 hexagonal cell. For the structural relaxation a 3x3x1 Γ-centered k-point grid was used to sample the Brillouin zone.

The lattice parameters, volume and atomic positions were optimized for the bulk structure without defects. For the structures with defects, only the positions of the atoms in the three layers above and below the interstitial defect inside the VdW gap along the c-axis were optimized, as explained in more detail in the section 3.4. For the electronic self-consistency loop, convergence is achieved when the total free energy change and band structure energy change are both smaller than 10^{-5} eV between electronic steps. The structure is considered converged when the forces on the atoms are smaller than 0.01 eV/Å. Finally, an additional electronic optimization including spin-orbit coupling (SOC) was performed, based on the geometry obtained from the structural optimization and without using the VdW interaction.

The equilibrium concentration of a defect D is determined by the defect Gibbs free energy of formation $G_f[D]$ (Freysoldt *et al.*, 2014)

$$c \sim e^{-G_f[D]/k_B T} \qquad (1)$$

where $G_f[D]$ depends in principle on pressure P and temperature T, and k_B is Boltzmann's constant. However for solids this (P,T) dependence can be neglected in a first approximation (Freysoldt *et al.*, 2014) and $G_f[D]$ then reduces to the defect formation energy $E_f[D]$, which for a defect in a charge state q is defined by

$$E_f = E_{tot}[D] - E_{tot}[bulk] - \sum_i \Delta n_i \mu_i + q\,\mu_e\,, \quad (2)$$

where $E_{tot}[D]$ is the total energy of the structure with a defect and $E_{tot}[bulk]$ that of the ideal defect-free structure. Δn_i is the amount of added (positive) or removed (negative) atoms of element i, μ_i are the chemical potentials of element i (i =Bi, Se) and μ_e is the chemical potential of the electrons (the "Fermi energy"). Since the band gap of Bi_2Se_3 is rather small we limit ourselves to neutral point defects ($q = 0$) in this work (Hashibon & Elsässer, 2011).

The chemical potentials μ_i ($i =$ Bi, Se) reflect the influence of the reservoirs with which atoms are exchanged to create the defect and the actual value depends on the experimental growth conditions. The chemical potentials are considered as variables (Van de Walle & Neugebauer, 2004), but are subjected to several constraints. An upper bound follows from the fact that precipitation of the elemental phase should be avoided

$$\mu_i \leq \mu_i^0 \ (i = \text{Bi, Se})\,, \qquad (3)$$

where μ_i^0 is the chemical potential of the elemental phase and where e.g. $\mu_{Bi} = \mu_{Bi}^0$ corresponds to Bi-rich (or Se-poor) conditions.

The hexagonal R-3m structure (6 atoms) is used to calculate μ_{Bi}^0 and the trigonal $P3_121$ structure for μ_{Se}^0 (3 atoms) (West *et al.*, 2012; Hashibon & Elsässer, 2011). Hexagonal unit cells were chosen for

all materials (Bi_2Se_3, Se and Bi), resulting in a maximal error cancellation when the same k-point density in reciprocal space is used (Hashibon & Elsässer, 2011), leading to a 9x9x3 mesh for Bi and a 9x9x9 for Se.

Since the numerical value of μ_i depends on the used reference, we prefer to work with

$$\Delta\mu_i = \mu_i - \mu_i^0, (i = \text{Bi, Se}). \quad (4)$$

The formation enthalpy of Bi_2Se_3, defined by

$$\Delta H_f = E_{tot}[\text{Bi}_2\text{Se}_3] - 2\,\mu_{Bi}^0 - 3\mu_{Se}^0\,, \quad (5)$$

can then be rewritten as

$$\Delta H_f = 2\,\Delta\mu_{Bi} + 3\,\Delta\mu_{Se}\,. \quad (6)$$

In Eq. (5) $E_{tot}[\text{Bi}_2\text{Se}_3]$ is the total energy per formula unit. The upper bounds of Eq. (3) in combination with Eq. (6) provide also lower bounds for $\Delta\mu_{Se}$ and $\Delta\mu_{Bi}$,

$$\Delta\mu_{Bi} \leq 0 \Longrightarrow \Delta\mu_{Se} \geq \frac{1}{3}\Delta H_f\,. \quad (7)$$

$$\Delta\mu_{Se} \leq 0 \Longrightarrow \Delta\mu_{Bi} \geq \frac{1}{2}\Delta H_f\,. \quad (8)$$

The defect formation energy, given by Eq. (2), can be written in a more convenient form by using Eqs. (4) and (6),

$$E_f(\Delta\mu_{Se}) = E_f^0 - \frac{1}{2}\Delta H_f \Delta n_{Bi} + \left(\frac{3}{2}\Delta n_{Bi} - \Delta n_{Se}\right)\Delta\mu_{Se}\,, \quad (9)$$

where E_f^0 is the defect formation energy of Eq. (2) in function of the reference chemical potentials μ_{Bi}^0 and μ_{Se}^0. Equation (9) will be used later when discussing the various defects and shows that the defect formation energy depends linearly on the chemical potential $\Delta\mu_{Se}$. A similar expression can be derived for $E_f(\Delta\mu_{Bi})$.

Finally, the minimum energy path for certain defect migrations is calculated using the climbing image modification of the nudged elastic band (NEB) method (Henkelman & Jonsson, 2000*a*,*b*) using seven intermediate images between start- and final configuration with inclusion of the VdW interaction. Afterwards, SOC was applied to the images with the lowest and highest total energy in order to determine the energy barrier of the path including SOC but without optimizing the atomic coordinates or lattice parameters.

3. Results

3.1. STEM/EDX

Preparation techniques can introduce or affect defects, so we used two completely different sample preparations to rule out, as much as possible, the effects of sample preparation on our results. The stacking of the quintuple layers (QLs) is visible in the high-angle annular dark-field scanning transmission electron microscopy (HAADF-STEM) images along the [010] zone (Fig. 2). The samples contained the same defects, independently of the used preparation technique: Bi substituted at the Se outer layers of the QLs, interstitial defects in the Van der Waals (VdW) gap and interstitial defects in the middle and outer Se layers of the QLs. The first defect can be recognized by some atom columns in the outer Se layers (indicated by blue arrows in Fig. 2) being brighter than those in the central Se layers of the QLs. The grey scale of an atomic column in HAADF-STEM scales with the averaged atomic number Z of the atoms in that column. Thus, a Se column that contains Bi atoms at some of the Se positions appears brighter than a pure Se column (Fig. 3). The interstitial defects can be recognized by the appearance of extra dots in between the regular atom columns (magenta, green and yellow arrows in Fig. 2). The interstitial defects have a tendency to cluster. A similar example of cluster formation was found in $(Bi_{1-x}In_x)_2Se_3$ where substituted In atoms have this cluster inclination on the Bi positions (Sánchez-Barriga *et al.*, 2018), which is in agreement with the thermodynamical proneness to demix in the equilibrium phase diagram of Bi_2Se_3-In_2Se_3 (Bouanani *et al.*, 1996). The reason why the defects cluster in Bi_2Se_3 is not known. Comparison with HAADF-simulations suggests that the interstitial defect inside the VdW gap occupies an octahedral site rather than a tetrahedral site (Fig. 4f). We found Bi substituted on the middle Se layers only in the cryo-crushed sample, which might be because on the crushed particles we study the edges of the sample, while the FIB samples are made from sections through the bulk.

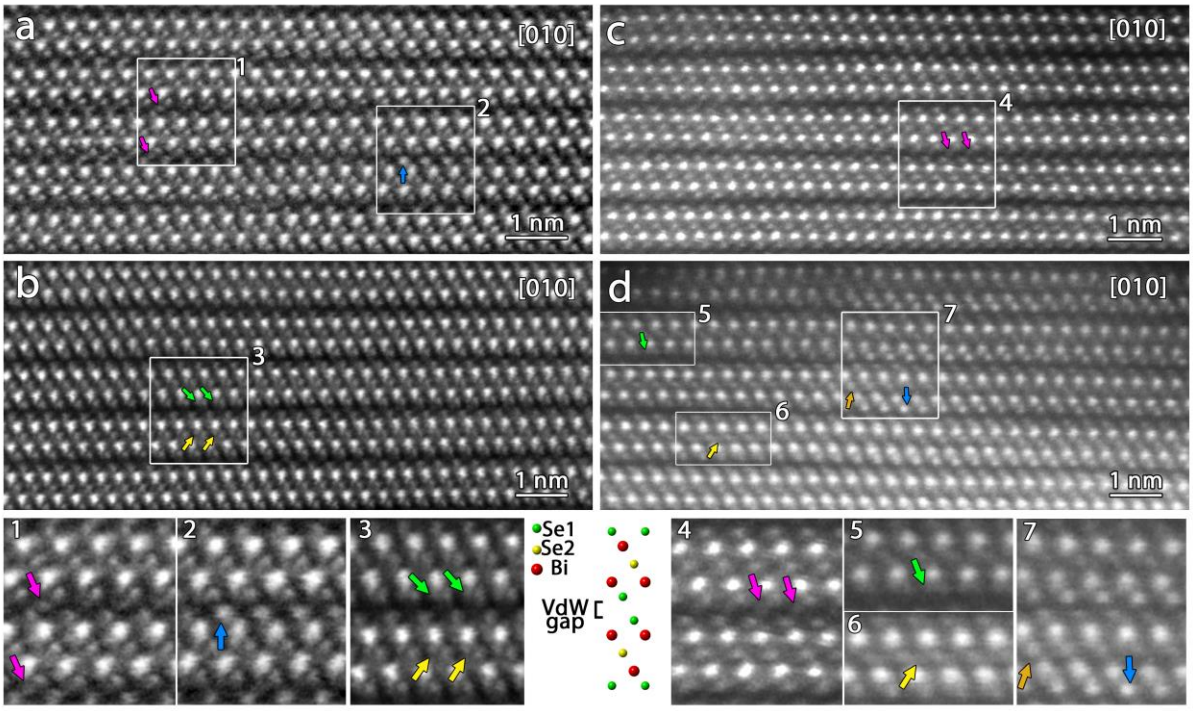

Figure 2 HAADF-STEM images from a FIB prepared sample (a. and b.) and a cryo-crushed sample (c. and d.), with magnified areas displayed at the bottom of the figure combined with a unit cell of a defect free structure at the same scale as the magnified images (1-7). Magenta arrows (1 and 4) mark the interstitial defects in the VdW gap. Yellow arrows highlight the interstitial atoms in the central Se layer of the quintuple layer (QL) (3 and 6) and green arrows in the outer Se layers (3 and 5). Bi also occupies Se sites in the outer Se layers of the QLs, indicated with blue arrows in 2 and 7. An orange arrow marks Bi in the middle Se layer (7).

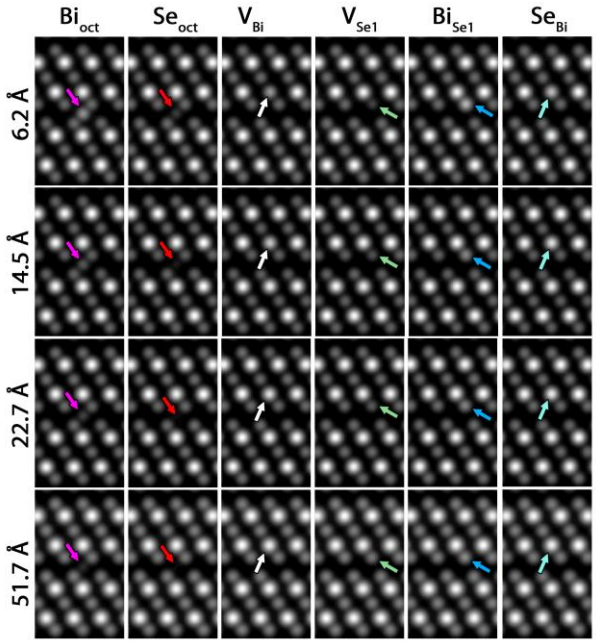

Figure 3 HAADF-STEM simulations using QSTEM (Koch, 2002) of different defects at different thicknesses when accounting for one defect: interstitial Se and Bi defects in the Van der Waals gap, Bi and Se vacancies and substitutional defects. An expected trend due to the Z dependency of HAADF-STEM images throughout the simulations is that the defects caused by Bi (Bi_{oct}, V_{Bi} and Bi_{Se1}) are more visible at the same thickness than the corresponding Se caused defects (Se_{oct}, V_{Se} and Se_{Bi}).

The interstitial defect in the VdW gap appears mobile in the cryo-crushed sample. Figures 4a-4b display one specific trajectory: an atom jumps from the Se outer layer through the VdW gap to the outer Se layer of the neighbouring QL, resulting in temporary interstitial defects in the VdW gap. The STEM-EDX map (Fig. 4d) shows that the chemical nature of this defect is mainly bismuth. Furthermore, if only one atom shifts its position, the movement of Bi would be more visible than of Se in a HAADF-STEM image, due to the lower Z value of Se (Fig. 3). The line profile of the STEM-EDX map shows several small Bi peaks away from the Bi layers of the ideal Bi_2Se_3 structure. The position marked on the EDX map (Fig. 4d) with a pink arrow shows a clear Bi signal at the octahedral position, however, the profile shows the corresponding peak shifted more towards the upper Se layer.

We propose that this apparent discrepancy is due to the mobility of the Bi atoms. In the EDX map, Bi is clearest where it does not overlap with the strong Se signal, but the profile cumulates the different signals of Bi along its path, undisturbed by the Se signal. Similarly the peaks of other interstitial positions deviate from their expected positions. One Se signal is present in the centre of the VdW gap in the line profile, and the outer Se layer of the QL above has a smaller peak height than the Se peak of the QL below (Fig. 4d). This suggests that Se moved from the Se layer above the VdW gap to the VdW gap. On the HAADF-STEM image of the EDX map the interstitial defects are not seen, because the HAADF-STEM image is only one instance of a time series of images of the area while the maps are the sum of the different scans of the area over the whole time interval. A small Bi peak, indicated with a Bi_{Se1} arrow, exists in the line profile at the same position as an outer Se peak, in Fig. 4d. The outer Se peak also has a lower signal in comparison to the other Se peaks, implying Bi substituted at the outer Se layer.

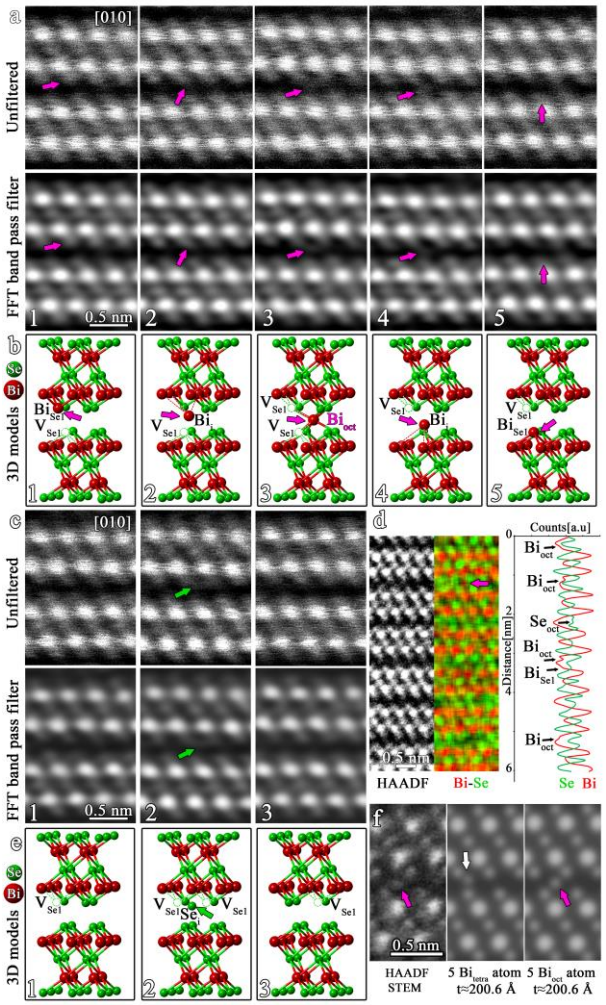

Figure 4 (a) Time series (every 20.1s) of the unfiltered (top) and FFT band pass filtered (bottom) HAADF-STEM images from the cryo-crushed sample along [010] of the temporary creation of an interstitial defect in the VdW gap, marked with magenta arrows. (b) Schematic model of the observation in Fig. 4a: a Bi atom at the Se1 position (Bi_{Se1}) (1) migrates toward the VdW gap, moving

through a temporal displaced non-octahedral site (Bi_i) (2) and finally creates a Se1 vacancy (V_{Se1}) and an interstitial Bi atom (Bi_{oct}) (3). Next, the atom goes to a non-octahedral site (Bi_i), removing the interstitial defect in the octahedral site (4) and jumps into a vacancy in the neighbouring Se layer (5). (c) Time series (0s, 40.2s, 60.3s) of the unfiltered (top) and FFT band pass filtered (bottom) HAADF-STEM images from the cryo-crushed sample along [010] of the temporary creation of an interstitial defect inside the Se1 layer, marked with green arrows. (e) Schematic model of the observation in Fig. 4c: a Se atom displaces from its original position (1), creating a vacancy and an interstitial atom in the Se layer (2), the interstitial atom occupies the neighbouring Se vacancy (3). The direction of vacancy diffusion is indistinguishable from the HAADF-STEM images. (d) HR-EDX map. Bi occupies the interstitial position in the VdW gap (magenta arrow). In the line profile three types of defects are visible: Bi_{oct}, Se_{oct} and Bi_{Se1} (black arrows). (f) HAADF-STEM (left, smaller area of Fig. 2a.1) with simulated images using QSTEM (Koch, 2002) of zone [010] with five Bi atoms at the tetragonal site (Bi_{tetra}) (middle, white arrow) and five at the octahedral site (right, magenta arrow) in the VdW gap to verify the coordination of the interstitial defect. The thickness of the simulated samples is 200.6Å, a realistic thickness for a FIB sample prepared as described in the method section (Bals *et al.*, 2007). The edges of a crushed sample can be as thin as a few Å. The amount of defects is chosen in such a way that the relative contrast of all columns is similar to the experimental image for a sample thickness of 200.6Å.

The interstitial defect in the outer Se layers of the QL is also mobile, observed for the cryo-crushed sample: an atom jumps briefly in an interstitial position and disappears again (Fig. 3c and 3e). The observed path deviates slightly from the linear path between the start- and end configuration; a small deviation towards the VdW gap is visible. We could not determine the chemical character of this defect with EDX due to the small interatomic distances in the Se layer. Presumably, mainly Se occupies this interstitial defect, because of the dominant Se character of this layer. Of course, the argument that a moving Bi atom is more easily observable than a moving Se atom due to the Z contrast of a HAADF-STEM image also applies here (Fig. 3).

As high resolution STEM imaging is known to cause defects by itself in other compounds (Meyer *et al.*, 2012; Zhu & Botton, 2015; Jiang, 2016; Egerton *et al.*, 2004), we decided to supplement these images by determining the structure from quantitative electron diffraction data, as this type of data can be taken at a much lower electron dose rate, allowing to accurately solve the structure of even very beam sensitive materials, like hydrogen storage materials, organic materials, pharmaceuticals and proteins (Kolb *et al.*, 2007; van Genderen *et al.*, 2016; Nederlof *et al.*, 2013).

3.2. PEDT

The crystal used for PEDT had a diameter of ~200nm. Dynamical refinement was essential due to the heavy elements. We started the dynamical refinement from the ideal Bi_2Se_3 structure without defects

and determined a rough estimate for the global thickness parameter for the dynamical refinement from low magnification TEM images of the crystal taken every 5°. To know the thickness of the sample at 0° tilt angle, we require a TEM image at 90°. However, the maximum tilt angle limit was 76°. From every TEM image, the projected width is determined by calculating the area of the crystal divided by its length. Next we extrapolate the determined projected width values to 90° to obtain an estimate for the final thickness, namely 367 Å. The same thickness was used for all diffraction patterns. Determining the thickness parameter experimentally was a crucial factor for the successful refinement as the thickness plots generated by Dyngo of the diffraction patterns led to a different thickness parameter (~50-200 Å). We decided to use the one determined directly from the low magnification images.

Refining the Se occupancies suggest the presence of Bi on these Se sites, Bi_{Se}, as the occupancy refinement consistently gives an occupancy >1 for these positions. We speculate that an even higher Bi concentration is present on these sites, as several examples in the literature indicate the existence of Se vacancies, especially on the outer Se layers of the quintuple block (Dai *et al.*, 2016; Scanlon *et al.*, 2012; Unzueta *et al.*, 2016; Devidas *et al.*, 2014; Alpichshev *et al.*, 2012; Mann *et al.*, 2013; West *et al.*, 2012; Wang *et al.*, 2013; Xue *et al.*, 2013). Vacancies could not be taken into account, because an unknown amount of vacancies on the already mixed Bi_{Se1}/Se1 sites leaves too many degrees of freedom (an excess of Bi can be compensated by more vacancies). The displacement parameters of elements on the same crystallographic site are constrained to be equal, neglecting the chemical dependence. This limits the number of parameters and is a reasonable approximation in EDT, where the determination of displacement parameters is less accurate compared to techniques as SXRD. Moreover, the occupancy of Bi on the Bi sites of the basic Bi_2Se_3 structure was fixed to one to avoid a meaningless value higher than one.

The obtained difference Fourier map (F_{obs}-F_{calc}) suggests that there are interstitial atoms on the octahedral sites inside the VdW gap and in a distorted octahedral site between the inner and outer Se layers, positioned close to the Bi layers (Fig. 5). The obtained signal at these positions is higher than three times the standard deviation (3σ) of the difference Fourier map. The coordinates of this intermediate model are shown in Table 2. We propose Bi as the chemical character for both interstitial sites, respectively labelled from now on as Bi_{oct} and Bi_{int}. For the octahedral site inside the VdW gap, we base this decision on the STEM and EDX data. For the interstitial position inside the QL, the distance between the interstitial defect inside the QL and the closest Bi atom (2.39Å) is too small for an interstitial Se or Bi atom. We therefore suggest that Bi occasionally moves from its ideal position towards the interstitial position, so that both sites are not occupied at the same time. The sum of the occupancy of the Bi position in the ideal structure and the interstitial Bi inside the QLs was thus fixed to one. The atoms in the outer Se layers are less tightly bound due to the weak VdW interaction on one side, leading to the highest displacement parameters for this structure. The observed movement of

the interstitial defects indicate high displacement parameters and weaker bonding, which is similar to the outer Se site. So, the displacement parameters for the interstitial defects were restricted to the displacement parameters of Se1 and Bi_{Se1}. Up to this point, we constrained the coordinates of Se_1 and Bi_{Se1} to be identical. By removing this constraint, the Bi_{Se1} defect moves ~0.5Å towards the VdW gap. This movement is in agreement with the DFT calculations in section 3.4 (Fig. 8).

The refined structure with interstitial defects suggests 1.5(6)% Bi on the octahedral site in the VdW gap and 1.9(5)% on the interstitial position inside the QLs (Table 3). The reliability factors improve with only about 1%, probably due to the low quantity of defects (Table 6).

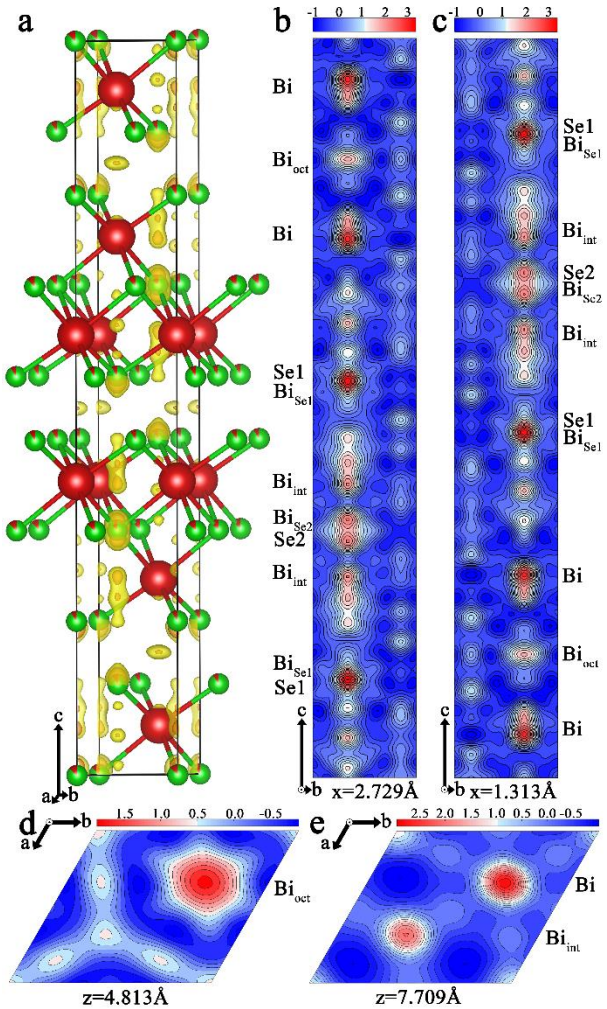

Figure 5 (a) 3D-difference Fourier map overlaid with the basic Bi_2Se_3 structure model including Bi substituted on the Se sites but without interstitial defects (Table 2) (Green spheres are Se; red spheres are Bi), plotted using VESTA (Momma & Izumi, 2011). The yellow (orange) areas contain values that are higher than 2σ (3σ) with σ the standard deviation, equal to 1.99e/Å. (b-c) 2D-difference Fourier map of the b-c plane at respectively x=2.729Å and x=1.313Å. (d-e) 2D difference Fourier map of the a-b plane at respectively z=4.813Å and z=7.709Å.

Table 2 Model from EDT based on the dynamical refinement with Bi substituted on the Se sites, Bi_{Se1} and Bi_{Se2}.

Atom	Occupancy	X [Å]	Y[Å]	Z[Å]	U_{iso}[Å²]
Bi	1	0	0	0.40045(11)	0.0228(3)
Se2	0.87(2)	0	0	0	0.0246(15)
Bi_{Se2}	0.13(2)	0	0	0	0.0246(15)
Se1	0.906(17)	0	0	0.20997(17)	0.0273(13)
Bi_{Se1}	0.094(17)	0	0	0.20997(17)	0.0273(13)

Table 3 Model from EDT based on the dynamical refinement with Bi substituted on the Se sites (Bi_{Se1} and Bi_{Se2}) and interstitial defects (Bi_{oct} and Bi_{int}) in an octahedral site in the VdW gap and in a distorted octahedral site in the QL layer.

Atom	Occupancy	X [Å]	Y [Å]	Z [Å]	U_{iso} [Å²]
Bi	0.974(10)	0	0	0.40034(11)	0.0225(5)
Se2	0.92(3)	0	0	0	0.0243(16)
Bi_{Se2}	0.08(3)	0	0	0	0.0243(16)
Se1	0.91(2)	0	0	0.2122(5)	0.0268(11)
Bi_{Se1}	0.09(2)	0	0	0.198(2)	0.0268(11)
Bi_{oct} in VdW	0.015(6)	0	0	0.5	0.0268(11)
Bi_{int} in QL	0.019(5)	0.333333	0.666667	0.606(6)	0.0268(11)

3.3. XRD

In order to compare the results to more standardly used techniques, we also performed XRD analysis of the crystals.

We tried single crystal XRD, however the five different sample preparation methods we tried were all unsuccessful. All resulted in badly crystalline samples which showed smeared out reflections on the single crystal XRD patterns. For the first method, we cooled the sample with liquid nitrogen and used a combination of manual cutting and a Well diamond wire to cut a small crystal from the bulk material. For the second method, we manually cut a crystal while submerging the sample in liquid nitrogen. For the third method, we used tape to remove a small piece of the sample; afterwards the fragments were disconnected from the tape by resolving the glue with dichloromethane, followed by

ultrasonic bathing in ethanol for 60 seconds. For the fourth sample, we performed cryo-crushing. For the fifth method, we tried to chemically remake the Bi_2Se_3 sample in a small enough size with the same sample preparation as mentioned in the methodology section, but the resulting crystallite size was unavoidably larger than required for SXRD (0.15-0.2mm). Therefore we turned to powder XRD.

We tested two different sample preparation methods. The sample prepared by ultrasonic bathing contained a very high $1\bar{1}5$ reflection compared to the calculated pattern using the ideal Bi_2Se_3 structure. Mixing starch underneath the sample proved this was caused by a preferential orientation, as the intensity of this peak decreased in the patterns taken after such addition. However, the starch introduced a high background at low 2θ-angles, making the patterns with less preferential orientation unusable. In the cryo-crushed sample the preferential orientation was less pronounced compared to the Bi_2Se_3 sample made by ultrasonic bathing without starch addition. Therefore, data treatment was only performed on the best data set, that of the cryo-crushed sample.

The ideal quintuple layered structure was the starting model for the Rietveld refinement. The displacement parameters for both Se layers were constrained to be identical due to the negative displacement parameter for Se2 when refined separately. Refining the occupancies of both Se positions resulted in an occupancy value higher than 1, so Bi was added to these sites. The occupancy of Bi_{Se2} was 0.061%, whereas for Bi_{Se1} only 0.004%. The occupancy for the Bi site was kept fixed at 1, due to its unrealistic value (>1). Next, preferred orientation along the [$\overline{2}0$ 20 3] direction, using the March-Dollase approach, was included to account for the unusually high $1\bar{1}5$ reflection. Preferential orientation along the c-axis provided a worse visual fit of the PXRD profile and this option was thus discarded. Further refinement led to a negative Bi_{Se2} occupancy, resulting in the removal of Bi_{Se2} and the restriction of the Se2 occupancy to 1. This intermediate model is shown in Table 4. Also, harmonic, anisotropic displacement parameters were tested (Table 5). Separate refinement of the Se1 and Bi_{Se1} coordinates moved the substituted Bi toward the QL instead of towards the VdW gap, which is in disagreement with EDT and DFT. Therefore, the coordinates of both elements were held constrained. No signs of any interstitial defects were observed during this refinement. The final fit is shown in Fig. 6.

Next, to compare, we used the EDT models with and without interstitial defects inside the VdW gap and QLs to fit the PXRD data, restarting from the original Le Bail fit. All profile parameters, including the cell parameters, were refined and the same preferential orientation direction was again introduced. The R factors of these models were worse compared to the model found from PXRD (Table 6).

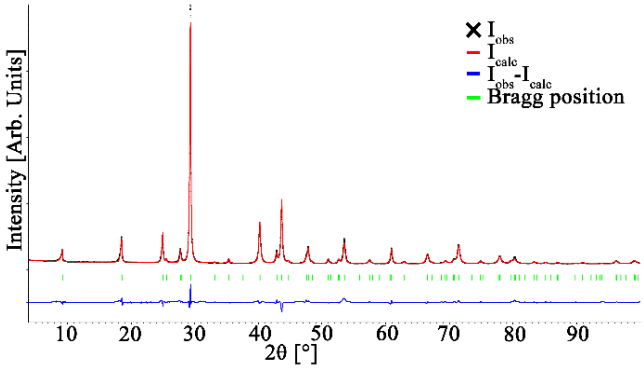

Figure 6 Observed PXRD spectrum (black), with its fit (red) where the PXRD model with anisotropic displacement parameters is used (Table 5). The difference between both is displayed at the bottom.

Table 4 Model from PXRD with isotropic displacement parameters.

Atom	Occupancy	X [Å]	Y [Å]	Z [Å]	Uiso [Å²]
Bi	1	0	0	0.40037(4)	0.0092(3)
Se2	1	0	0	0	0.0105(7)
Se1	0.984(3)	0	0	0.21063(6)	0.0105(7)
Bi_{Se1}	0.016(3)	0	0	0.21063(6)	0.0105(7)

Table 5 Model from PXRD with harmonic, anisotropic displacement parameters.

Atom	Occupancy	X[Å]	Y [Å]	Z [Å]	U_{ani} [Å²]
Bi	1	0	0	0.40052(4)	0.0112(4)
Se2	1	0	0	0	0.0192(9)
Se1	0.988(2)	0	0	0.21014(7)	0.0192(9)
Bi_{Se1}	0.012(2)	0	0	0.21014(7)	0.0192(9)

Atom	U_{11} [Å²]	U_{22} [Å²]	U_{33} [Å²]	U_{12} [Å²]	U_{13} [Å²]	U_{23}[Å²]
Bi1	0.0034(3)	0.0034(3)	0.0267(9)	0.00168(17)	0	0
Se1/Se2/ Bi_{Se2}	0.0044(6)	0.0044(6)	0.049(2)	0.0022(3)	0	0

Table 6 Differences in cell parameters and reliability factors for different models.

	PXRD					EDT	
	Le Bail fit of the PXRD data	Model Table 5	Model Table 4	Model with only Bi_{Se1} and Bi_{Se2} (Table 2)	Model with Bi_{Se1} and Bi_{Se2}, Bi_{oct} and Bi_{int} (Table 3)	Model with only Bi_{Se1} and Bi_{Se2} (Table 2)	Model with Bi_{Se1} and Bi_{Se2}, Bi_{oct} and Bi_{int} (Table 3)
Chemical formula		$Bi_{2.024}Se_{2.976}$	$Bi_{2.032}Se_{2.968}$	$Bi_{2.318}Se_{2.682}$	$Bi_{2.261}Se_{2.740}$	$Bi_{2.318}Se_{2.682}$	$Bi_{2.261}Se_{2.740}$
a [Å]	4.140961(25)	4.14070(3)	4.14078(4)	4.14006(10)	4.14004(10)	4.1407	4.1407
b [Å]	4.140961(25)	4.14070(3)	4.14078(4)	4.14006(10)	4.14004(10)	4.1407	4.1407
c [Å]	28.65922(44)	28.6564(6)	28.6579(6)	28.6475(12)	28.6479(11)	28.6564	28.6564
R (F_0) [all/obs]		4.37/4.37	6.40/6.40	9.15/8.80	8.47/8.11	28.73/14.86	28.08/14.23
wR(F_0) [all/obs]		5.96/5.96	8.06/8.06	12.07/12.03	11.49/11.46	16.61/16.13	15.92/15.44
R_p	2.24	3.13	3.70	4.75	4.61		
R_{wp}	3.45	4.70	5.41	6.89	6.66		
χ^2	8.87	12.06	13.89	17.69	17.10	6.57/9.49	6.34/9.15

3.4. DFT

For the structure optimization with defects, all atoms in the 3x3x1 cell are fixed except for the 6 layers along the c axis around the interstitial defect. Optimizing all atomic positions causes a small displacement of the two complete QL blocks around the interstitial defect, which corresponds more to a defect structure rather than a rare local defect. The binding forces between the atoms in the QL are significantly higher than the weak VdW interaction, causing the QLs to displace when all atomic positions are allowed to optimize within the periodic boundary conditions of VASP. The energy difference of the optimized intermediate configuration with two vacancies and a Bi atom in the octahedral site corresponding to the saddle point of Fig. 8c with and without fixing the chosen positions is 117 meV for the complete 3x3x1 cell or ~0.9 meV per atom. We also tested the influence of fixing the atomic positions on the energy barrier. For comparison, the path displayed in Fig. 8c has an energy barrier of 1.716 eV when optimizing all atoms versus 1.766 eV when optimizing only the

atomic coordinates of the atoms in the six layers closest to the defect. This indicates that fixing the atomic positions of the atomic layers has only a minor influence on the kinetic barriers of the defect migrations. Furthermore, only the octahedral interstitial site in de VdW gap (and not the tetrahedral one) was studied, based on the STEM and EDT data.

Using Eq. (5) (section 2.4) we obtain a formation enthalpy (per formula unit) for Bi_2Se_3 of -1.83 eV including SOC, and -1.96 eV without SOC. Both values agree well with the experimental result of -1.60(17) eV (at 298K) with a somewhat better agreement for the SOC calculation (Semenkovich & Melekh, 1972). Furthermore, we calculated the defect formation energy using Eq. (9) (section 2.4). We use the Se-poor regime to compare the calculated formation energies to the experimental defect occupancies derived from our EDT results (section 4), because during the sample preparation a stoichiometric ratio of Bi and Se was used and Se loss is expected due to the gaseous nature of Se at 800°C. The evacuated sealed silica tube helps to prevent Se loss, but stoichiometric values are difficult to obtain. This suggests rather Se-poor than Se-rich conditions. Figures 7c-7d show the formation energies of different single defects without and with including spin-orbit coupling (SOC): Bi substituted on Se1 and Se2 (Bi_{Se1} and Bi_{Se2}), Se substituted on Bi (Se_{Bi}), Se1 and Se2 vacancies (V_{Se1},V_{Se2}), Bi vacancies (V_{Bi}) and interstitial Bi and Se inside the VdW gap (Bi_{oct} and Se_{oct}). For the Se-poor regime, Bi_{Se1} has the lowest formation energy, followed by V_{Se1}, V_{Se2}, Bi_{Se2}, V_{Bi} and Bi_{oct} when we include SOC. Without SOC, V_{Bi} is removed from this ranking. For the Se-rich limit, V_{Bi} has the lowest formation energy when including SOC, followed by Se_{Bi}, V_{Se1}, V_{Se2}, Se_{oct}, Bi_{Se1}, Bi_{oct} and Bi_{Se2}. Without SOC, Se_{Bi} has the lowest formation energy, followed by V_{Se1}, V_{Se2}, Bi_{Se1}, V_{Bi}, Se_{oct}, Bi_{Se2} and Bi_{oct}. In case of the Se-rich limit (or Bi-poor limit) the SOC results seem intuitively more logical: if more Se is present, it is more likely that Bi vacancies exist and that Se substitutes Bi. When SOC is neglected, however, Se1 vacancies are second in the ranking of having the lowest formation energy. Also, Se_{oct} is lower in the ranking in the calculation with SOC compared to the calculation without SOC. In general, we notice a strong decrease in formation energy for V_{Bi} for the results including SOC.

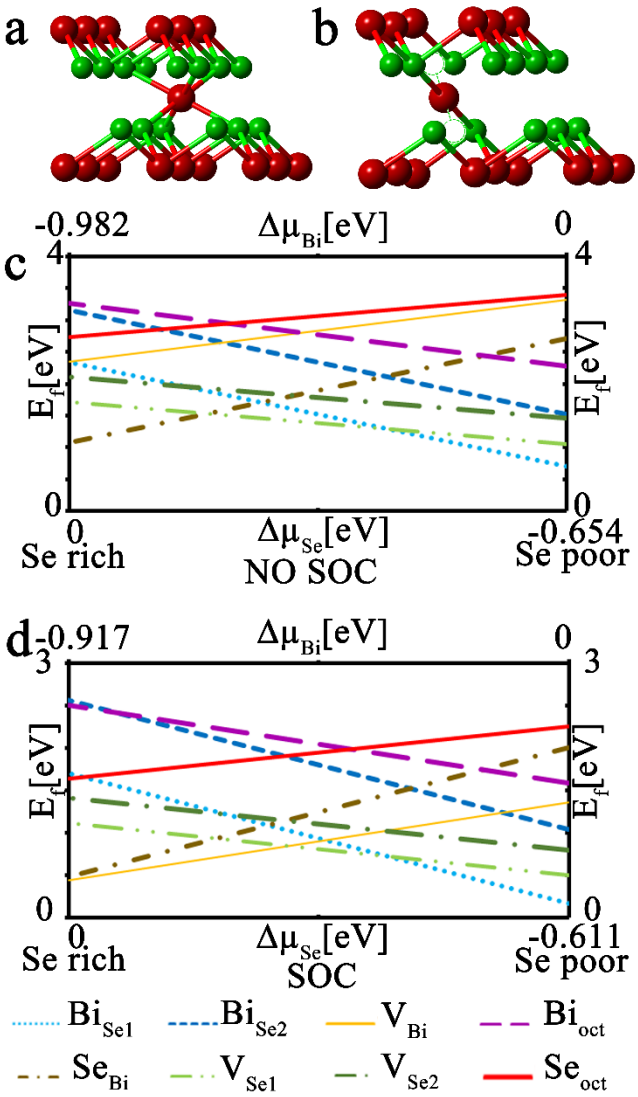

Figure 7 Bi coordination for an octahedral site (a) and a planar site (b) in the VdW gap. The Bi-Se bonding distance is ~2.7 Å for the octahedral site in (a). The V_{Se1}-Bi distance is ~1.8 Å and the Bi-Se bonding distance is ~3.4 Å for the planar site in (b). Defect formation energies as a function of the chemical potentials $\Delta\mu_{Bi}$ and $\Delta\mu_{Se}$ without (c) and with (d) including SOC.

To study the migration of defects across the VdW gap and inside the Se1 layer, several paths between different configurations of vacancies were studied, where crystallographically equivalent paths were assumed equal. For every crystallographically distinct two vacancy configuration, combined with an interstitial defect in an octahedral setting inside the VdW gap, the total structure is optimized. Except for one configuration for an interstitial Bi atom (Fig. 7b), all final geometries correspond to a distorted octahedral configuration (see Fig. 7a for the octahedral site). This planar configuration is only possible due to the free space provided by the vacancies. Paths passing through the distorted octahedral site and linear paths between two Se vacancies in an adjacent or the same Se layer were studied. When the octahedral position does not lie on the linear path between the two Se vacancies, we always interpolate via the optimized intermediate structure when setting up the initial path. One Bi

path (Fig. 8b) is an exception to the latter. When we optimized the intermediate position (two Se vacancies and one Bi atom on the octahedral site) of the path shown in Fig. 8b the interstitial Bi moved to a planar configuration (Fig. 7b). Because we are interested in the migration of Bi along the octahedral site, we constructed an initial path along this octahedral site. Furthermore, to speed up convergence we used the FIRE force based optimizer (Sheppard *et al.*, 2008). However, as the path converged to the path displayed in Fig 8a, we fixed Bi on the octahedral site, resulting in the optimized path shown in Fig. 8b.

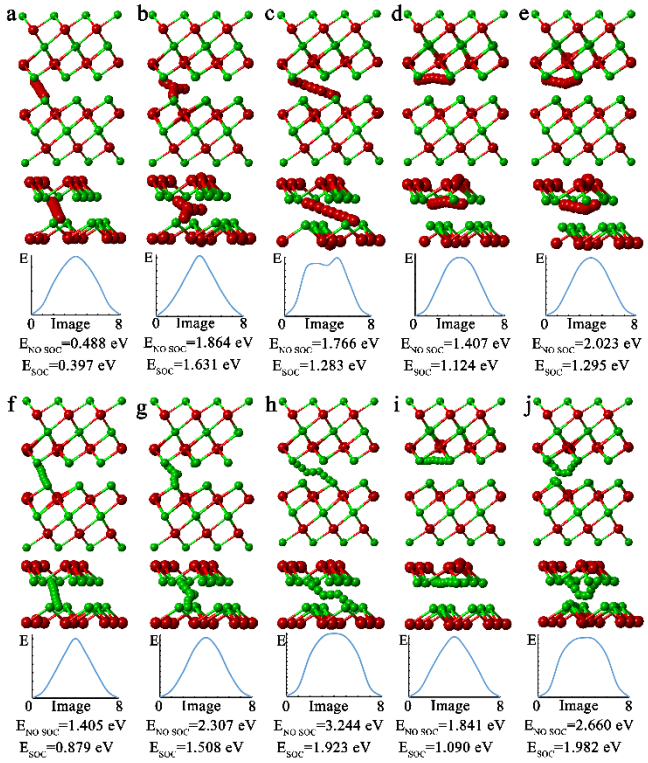

Figure 8 Top row (a-e): Different migration paths for Bi_{Se1} diffusion towards the Se1 layer on the opposite side of the VdW gap or towards a neighbouring Se1 vacancy in the same layer. Middle row (f-j): Se1 diffusion towards the VdW gap to the opposite Se1 layer or towards a neighbouring V_{Se1} vacancy in the same layer. For every migration path (top to bottom) the projected structure along the **b** axis is displayed, then a close up of the environment around the moving atom, followed by a plot displaying the total energy change for the images along the path with the calculated energy barrier with and without including SOC. For the models itself, the positions of all atoms of the nine images of the migration path are integrated into one image.

When including SOC, a diffusing Bi atom needs to overcome an energy barrier of 1.283 eV or 1.631 eV to jump towards a V_{Se1} in the adjacent layer along the Bi_{oct} position. Without SOC, the corresponding energy barriers are 1.766 eV and 1.864 eV. The linear Bi path along the planar position has a low energy barrier of only 0.397 eV with SOC and 0.488 eV without SOC. A calculated energy barrier including SOC of 1.124 eV or 1.295 eV, respectively for a linear path and a path passing

through a distorted octahedral position, should be overcome to allow a Bi atom to jump to a neighbouring Se position inside the same Se layer. Without SOC, the energy barriers are respectively 1.407 eV and 2.023 eV. In general, the energy barriers for Bi and Se become significantly lower on including SOC. These energy barriers, especially the ones including SOC, are similar or even lower than those found for α-GeTe, which has a comparable structure with a two-layered block of Ge and Te with weak VdW interactions in between. There, the activation barriers for Ge diffusion using also a vacancy mechanism range from 0.95 eV to 2.44 eV, depending on the path (linear or curved) and the number of Ge vacancies present (Ge vacancies helped to decrease the barrier) (Deringer *et al.*, 2013). As a rule of thumb, reactions with an energy barrier of 21 kcal/mol (≈0.9 eV per atom) or lower, will happen readily at room temperature (Young, 2001; Dai *et al.*, 2013). An activation barrier of 1.4 eV was also experimentally determined for Ge diffusion, probably by a vacancy mechanism, inside PbTe (Yashina *et al.*, 1997).

Similar trajectories are found for a migrating Se atom. The energy barriers to jump towards the adjacent Se layer are higher than for a Bi atom, except for the Se path displayed in Fig. 8g when including SOC. The latter can be explained by the required fixation of Bi on the octahedral site for the corresponding Bi path (see Fig. 8b). The fact that the activation energy for a Se migration across the VdW gap is generally higher than that of the corresponding Bi path agrees with our expectations: more energy is required to remove a Se atom from its ideal position in the bulk structure than for a Bi_{Se1} defect. This is also clear from the amount of energy necessary to move a Bi or Se atom from the Se1 layer towards the octahedral interstitial position: 2.149 eV without SOC or 1.687 eV with SOC for a Bi atom and respectively 3.677 eV and 2.537 eV for a Se atom. However, the energy barrier for a Se atom to linearly jump to a neighbouring V_{Se1} position inside the same Se layer (Fig. 8i) is lower than for Bi when including SOC, probably due to its smaller size and thus smaller local distortion. Note that for the non-linear path of the Se atom jumping to a neighbouring Se vacancy of the same Se layer along an octahedral site (Fig. 8j), the FIRE force-based optimizer was used. The interstitial Se_{oct} at the saddle point forms a Se-Se bond with a Se1 atom of the adjacent layer of size 2.37 Å (standard Se-Se bonding is ~2.4 Å). This path has a high energy barrier compared to the corresponding Bi path.

4. Discussion

With STEM we observed interstitial defects inside the VdW gap with mainly Bi character determined by EDX. Both samples prepared with different methods contained these defects, suggesting that they are not induced by sample preparation. Moreover, through simulations using QSTEM (Koch, 2002), we verified that one Bi atom in the VdW gap is indeed still detectable in STEM images of thin samples of around 50 Å (a thickness very well possible for imaged areas in cryo-crushed samples) in the [010] zone. The fact that the defects are also observed in EDT performed with a parallel, spread electron beam, i.e. at a much lower electron dose rate, supports that these defects are not simply

induced by the electron beam. Furthermore, the calculated defect formation energies support the EDT results.

We use the Se-poor regime to compare the calculated formation energies to the experimental defect occupancies derived from our EDT results, which is reasonable considering the volatile nature of Se (Hu *et al.*, 2014). Bi_{Se1} has the lowest formation energy for a Se-poor sample, followed by V_{Se1}, V_{Se2}, Bi_{Se2}, V_{Bi} and Bi_{oct} when we include spin-orbit coupling. Without SOC, V_{Bi} is removed from this ranking. Of the calculated single defects, Bi_{Se1} is indeed the defect present with the highest occupancy in EDT, followed by Bi_{Se2} and Bi_{oct}. Vacancies could not be taken into account, since the mixed occupancy of a site by Se, Bi and vacancies would supply too many refinable parameters. All defects except the vacancies are also observed with STEM. The fact that the vacancies were not observed does not mean they are absent, however, to count the atoms in a column from HAADF-STEM images, one needs a binary possibility for the occupation, and, also here, the possibility to have Se, Bi or a vacancy at each position prevents quantification. For PXRD only the defect with the lowest formation energy is found i.e. Bi_{Se1}. So, PXRD does not indicate the presence of interstitial defects. However, we are inclined to consider the EDT data as more reliable for several reasons. First, the EDT data is measured from a single crystal. Second, the preparation of the sample for PXRD was challenging: all samples had a preferential orientation, which makes Rietveld refinement more difficult since a preferred orientation influences the peak intensity, next to anisotropic peak broadening (caused for example by an anisotropic sample size or complex defect structure). Moreover, in our attempts to collect single crystal X-ray data we observed reduced crystallinity after the application of any type of mechanical stress or size reduction, which implies that the crystallinity in the crystallites in the powder sample is probably also reduced. For EDT, on the other hand, we can filter out a perfect crystal that was not damaged during sample preparation. In PXRD this is not possible: the data is taken from the whole crushed sample, and for single crystal XRD, we did not succeed in creating a sufficiently undamaged crystal with a suitable size (≈0.15 mm per dimension).

Our findings on the interstitial Bi atoms in the VdW gap are also supported by the computational results of Tumelero *et al.* (Tumelero *et al.*, 2016) who found that the Bi interstitial defect in an octahedral setting has the lowest formation energy in a Se-poor material and the lowest or second lowest in a Se-rich material depending on the simulation settings. Jia *et al.* (Jia *et al.*, 2014) and Urazhdin *et al.* (Urazhdin *et al.*, 2002) propose the existence of interstitial Bi through indirect evidence. However, Dai *et al.* (Dai *et al.*, 2016) suggested the existence of interstitial Se atoms, where the concentration of interstitial Se increased for samples synthesized under Se-rich conditions. This is in line with our results for the calculated formation energies. The synthesis procedure clearly influences the presence of defects. This can explain why we observed a Bi dominant character for the interstitial defects, whereas Dai *et al.* found Se interstitial defects. So, STEM and EDX show the

existence of interstitial Bi defects in the VdW gap and both the EDT and DFT results support that they are not beam induced.

Based on the calculations of the transition state including SOC, we expect the Bi and Se migration paths in respectively Fig. 8a and 8f to occur easily and in Fig. 8i to happen exceptionally at room temperature. The Bi and Se path across the VdW gap have a calculated energy barrier of 0.397 eV and 0.879 eV respectively, which is lower than the rule of thumb energy barrier of 21 kcal/mol (≈0.9 eV per atom), at which the transition will happen readily at room temperature (Young, 2001; Dai *et al.*, 2013). The Se path inside the Se layer is 1.090 eV, which is slightly higher than 0.9 eV. The diffusion coefficient *D* is described by the Arrhenius equation (Car *et al.*, 1984; Shackelford, 2005; Wang *et al.*, 2011):

$$D = D_0 e^{-E/k_B T}, E = E_m + E_{f_v} \qquad (10)$$

with D_0 a pre-exponential factor, T the temperature, k_B Boltzmann's constant and E the activation energy, where the latter is the sum of the energy barrier E_m and the formation energy E_{f_v} of a vacancy in case of a vacancy mechanism. The formation energy is included in the equation because a vacancy should be present in the adjacent layer in order to jump toward this site, which has a probability proportional to $e^{-E_{f_v}/k_B T}$. From Eq. (10), we estimate that migrations along the Se path inside the Se layer occur about 1000 times less frequently than something that should happen readily. Without SOC, only the Bi path in Fig. 8a can exist easily at room temperature. Reasons why we did not directly observe Se movement within the outer Se layers (Fig. 8i) and Bi and Se migration across the VdW gap (Fig. 8a and 8f) calculated with SOC or only the Bi path (Fig. 8b) without SOC include the limited resolution of the microscope, the possibility that this migration is too rapid for us to record, or, in case of the Se path, that the Z value is too low to see the movement of one Se atom considering the thickness of the sample.

The observed path in Fig. 4c can correspond to the model of Fig. 8e, whereas the path in Fig. 4a can correspond to the model in Fig. 8b or 8g. The similarity of the paths in Fig. 8e and 8i is high, except for the slight deviation of the atom of the path in Fig. 8e towards the VdW gap. The latter combined with the fact that a moving Bi atom is more readily visible in STEM than a moving Se atom, suggests that we observed in Fig. 4c the path in Fig. 8e rather than 8i. This does not exclude that the path in Fig. 8i cannot happen, only that it is less probable that we observed it. For the observed path in Fig. 4a, one jumping Bi atom should be more readily visible in STEM, however for the calculated path in Fig. 8b the Bi atom in the octahedral site is fixed in order to force the path along this position. In the path in Fig. 8g a Se atom follows a similar route and for Se it is a true minimum energy path, however, the low Z value for Se suggests that multiple Se atoms should have moved at the same time for this to be visible. Due to the higher energy barriers of the paths in Fig. 8b, 8e and 8g, these

migrations are probably caused by the electron beam irradiation. Moreover, it is possible that these paths are more easily visualized in STEM due to their movement along the octahedral position, which is represented by a larger empty space than the shortest projected distance between the two opposing Se layers. Hence, the presence of an atom in the octahedral site is more easily recorded. In comparison, the atomic movement between atom columns that are closer together in projection could be more readily interpreted as noise. Even though the paths that are observed are likely to be influenced by the electron beam, the existence of these interstitial defects itself is probably not beam induced, because the interstitial Bi atoms are also observed using PEDT, which is considerably less beam damaging than STEM and EDX. The occupancy probability of the defects determined by EDT is also inversely proportional with their corresponding DFT calculated formation energies, which further supports the proposition that the interstitial defects are not merely a result of the electron beam.

The influence of the beam on the sample merits a detailed discussion. Ionization damage -causing radiolysis damage, thermal damage and electrostatic charging- and knock-on displacement damage are the main damage mechanisms inside a material due to the interaction with the electron beam (Egerton, 2019; Liu *et al.*, 2018). Beam damage depends on a lot of different parameters such as specimen thickness and orientation, beam voltage, beam current density and beam size (Jiang, 2016).

Radiolysis, electrostatic charging and heating are caused by inelastic scattering of electrons: the Coulomb interaction between the incoming electrons and the electrons of the atoms inside a material creates secondary electrons (Egerton *et al.*, 2004). The incident electron provides enough energy to remove an electron from the outer atomic shell (excitation) or inner atomic shell (ionization) of atoms, creating a vacancy and a secondary electron (Egerton, 2019). If this vacancy exists long enough, as it does in insulators and certain semiconductors, the ionized atom can move by breaking its chemical bonds, whereas movement is avoided when electrons fill this vacancy fast enough, as for metals (Egerton, 2019). The atom can only move when the excitation energy is changed into momentum due to thermal vibration and local Coulomb repulsion (Jiang, 2016; Hobbs, 1979). This is *ionization damage* or *radiolysis*. These secondary electrons can travel a few nanometers, creating even more damage (Egerton, 2019). For example, Hobbs proposed a model for the oxygen movement in tetrahedral silica due to radiolysis, where the oxygen in a Si-O bond moves off-centre and makes an O-O peroxy linkage, creating an O vacancy and interstitial (Hobbs, 1995). Cooling the sample can decrease radiolysis (Hobbs, 1990), but combining cooling with HAADF-STEM at high resolution is not yet possible. Many of the created secondary electrons due to the inelastic scattering have enough energy to leave the sample and can cause a local positive charge inside poorly conducting specimens, i.e. lead to *electrostatic charging*. This introduces an electric field that can cause atomic movement depending on the ionic and electrical conductivity of the material (Egerton, 2019; Hobbs, 1979). Furthermore, the local increase in temperature due to this inelastic scattering, i.e. the *heating* of the

sample, remains small, even when using STEM, due to its logarithmic dependence on the beam diameter (Egerton *et al.*, 2004; Egerton, 2019). For example, for silicon nitride the local temperature was increased with 2.0°C and 9.8°C for respective beam currents of 2.11nA and 10.31nA with a 300 nm beam diameter (Liu *et al.*, 2018), we used less than 50pA for atomic resolution STEM.

Knock-on damage inside the material and surface sputtering –respectively moving atoms inside the material or out of the material- are caused by elastic scattering of the electrons. Elastic scattering is an electron-nucleus interaction, inducing the incoming electrons to electrostatically deflect by the Coulomb field of the nucleus (Egerton *et al.*, 2004; Jiang, 2016; Egerton, 2019). The necessary displacement energy (E_d) depends on the bond strength, crystal lattice and atomic weight of the elements inside the material and the direction of the knock-on atomic momentum (Egerton, 2019; Egerton *et al.*, 2004). This mechanism is especially present in electrically conducting materials, like metals and some semiconductors (Egerton, 2019). When the transferred energy is high enough, the displaced atom can move to another (meta)stable site through a saddle point position, creating Frenkel pairs – a vacancy and an interstitial atom (Egerton, 2019).

Due to the small temperature rise, heating damage can be neglected in Bi_2Se_3. Furthermore, Bi_2Se_3 is not a poor conductor: at the surface, Bi_2Se_3 conducts and defects cause it to be slightly bulk conducting (Xia *et al.*, 2009; Hor *et al.*, 2009). The two mechanisms that are most likely to cause the observed movement of the defects in Bi_2Se_3 are knock-on damage and radiolysis. The Se atoms in the outer Se layers are on one side only weakly bound with VdW interactions, which makes them more vulnerable for knock-on damage. Radiolysis is also still an option, because the material is only slightly conducting in the bulk, which can cause the vacancy to not be filled in time, so that the atom can displace from its position.

We observed interstitial defects with mainly Bi character with STEM and EDX, supported with PEDT and the DFT calculated formation energy of the different defects. Intrinsic and native defects are an important topic, because they influence the materials properties and thus device-based applications. These defects also impact material engineering using doping, since doping can influence the formation energy of an intrinsic defect (Zhu *et al.*, 2016). Furthermore, DFT including SOC suggests that one Bi and Se path from one Se layer towards the adjacent Se layer can occur easily and the Se movement inside the outer Se layers is rather exceptional at room temperature. Without SOC, only the Bi path is easily present at room temperature. We have also shown that SOC strongly influences the energy barriers and formation energies. The formation enthalpy calculated with SOC agrees slightly better with the experiment. Knowledge about the mobility of atoms is necessary, because of its influence on many physical properties and processes, such as mechanical deformation and chemical degradation (Ramachandran *et al.*, 2017). Furthermore, information on the intrinsic migration of atoms around the VdW gap is specifically needed for battery applications (Ali *et al.*, 2013; Xu *et al.*, 2013; Xie *et al.*, 2018), because these migrations can tamper with the mobility of the dopants. Self-

diffusion gives us also a lower limit for the diffusion of dopants, when the dopants do not have excess charge and are smaller, and thus do not cause any lattice distortions (Fahey *et al.*, 1989).

5. Conclusion

We observed with high resolution-scanning transmission electron microscopy and high resolution-energy dispersive X-ray spectroscopy the presence of interstitial defects in the Van der Waals gap of Bi_2Se_3, independent of the sample preparation technique. Their observation is supported by a structural refinement based on precession electron diffraction tomography data, indicating that they are not merely induced by the electron beam. Furthermore, the defect occupancy probability determined by EDT is inversely proportional with their corresponding DFT calculated formation energies, excluding the vacancies which could not be taken into account in EDT due to the mixed occupancy (Bi, Se and vacancies) of the sites. These interstitial defects are at an octahedral site, occupied mostly by Bi atoms and only in rare cases by Se atoms. However, the paths that are energetically probable at room temperature (Se movement within the outer Se layers and Bi and Se migration across the VdW gap calculated with SOC or only the Bi path without SOC) were not observed directly in the TEM. Instead, the paths that were directly observed are less likely to occur according to DFT and thus those specific observed paths might be beam induced. We suggest that the energetically favourable paths were not observed because they need a higher resolution in both time and space than was available during the observations. Finally, we also have shown that SOC strongly influences the energy barriers and defect formation energies.

Acknowledgements We thank Artem M. Abakumov for providing the original Bi_2Se_3 sample and are also very grateful to Christophe Vandevelde for trying repeatedly to get good single crystal X-ray diffraction data out of each of our failed attempts at making an undeformed single crystal. The computational resources and services used in this work were provided by the VSC (Flemish Supercomputer Center) and the HPC infrastructure of the University of Antwerp (CalcUA), both funded by the FWO-Vlaanderen and the Flemish Government-department EWI.

References

Ali, Z., Cao, C., Li, J., Wang, Y., Cao, T., Tanveer, M., Tahir, M., Idrees, F. & Butt, F. K. (2013). *J. Power Sources*. **229**, 216–222.

Alpichshev, Z., Biswas, R. R., Balatsky, A. V., Analytis, J. G., Chu, J. H., Fisher, I. R. & Kapitulnik, A. (2012). *Phys. Rev. Lett.* **108**, 206402.

Ando, Y. (2013). *J. Phys. Soc. Japan*. **82**, 102001.

Bals, S., Tirry, W., Geurts, R., Yang, Z. & Schryvers, D. (2007). *Microsc. Microanal.* **13**, 80–86.

Blöchl, P. E. (1994). *Phys. Rev. B.* **50**, 17953.

Bouanani, H. G., Eddike, D., Liautard, B. & Brun, G. (1996). *Mater. Res. Bull.* **31**, 177–187.

Car, R., Kelly, P. J., Oshiyama, A. & Pantelides, S. T. (1984). *Phys. Rev. Lett.* **52**, 1814–1817.

Dai, J., West, D., Wang, X., Wang, Y., Kwok, D., Cheong, S.-W., Zhang, S. B. & Wu, W. (2016). *Phys. Rev. Lett.* **117**, 106401.

Dai, Y., Ni, S., Li, Z. & Yang, J. (2013). *J. Phys. Condens. Matter*. **25**, 405301.

Deringer, V. L., Lumeij, M., Stoffel, R. P. & Dronskowski, R. (2013). *Chem. Mater.* **25**, 2220–2226.

Devidas, T. R., Amaladass, E. P., Sharma, S., Rajaraman, R., Sornadurai, D., Subramanian, N., Mani, A., Sundar, C. S. & Bharathi, A. (2014). *EPL (Europhys. Lett.)*. **108**, 67008.

Dollase, W. A. (1986). *J. Appl. Crystallogr.* **19**, 267–272.

Egerton, R. F. (2019). *Micron*. **119**, 72–87.

Egerton, R. F., Li, P. & Malac, M. (2004). *Micron*. **35**, 399–409.

Fahey, P. M., Griffin, P. B. & Plummer, J. D. (1989). *Rev. Mod. Phys.* **61**, 289–384.

Finger, L. W., Cox, D. E. & Jephcoat, A. P. (1994). *J. Appl. Crystallogr.* **27**, 892–900.

Freysoldt, C., Grabowski, B., Hickel, T., Neugebauer, J., Kresse, G., Janotti, A. & Van de Walle, C. G. (2014). *Rev. Mod. Phys.* **86**, 253–305.

van Genderen, E., Clabbers, M. T. B., Das, P. P., Stewart, A., Nederlof, I., Barentsen, K. C., Portillo, Q., Pannu, N. S., Nicolopoulos, S., Gruene, T. & Abrahams, J. P. (2016). *Acta Crystallogr. Sect. A Found. Adv.* **72**, 236–242.

Han, J., Richardella, A., Siddiqui, S. A., Finley, J., Samarth, N. & Liu, L. (2017). *Phys. Rev. Lett.* **119**, 077702.

Han, N., Kim, S. I., Yang, J. Do, Lee, K., Sohn, H., So, H. M., Ahn, C. W. & Yoo, K. H. (2011). *Adv. Mater.* **23**, 1871–1875.

Hashibon, A. & Elsässer, C. (2011). *Phys. Rev. B - Condens. Matter Mater. Phys.* **84**, 144117.

Henkelman, G. & Jonsson, H. (2000*a*). *J. Chem. Phys.* **113**, 9901–9904.

Henkelman, G. & Jonsson, H. (2000*b*). *J. Chem. Phys.* **113**, 9978–9985.

Hobbs, L. W. (1979). *Introduction to Analytical Electron Microsopy*, Vol. edited by J.J. Hren, J.I. Goldstein & D.C. Joy, pp. 437–480. New York: Springer Science+Business Media.

Hobbs, L. W. (1990). *Scanning Microsc. Suppl.* **4**, 171–183.

Hobbs, L. W. (1995). *J. Non. Cryst. Solids*. **182**, 27–39.

Hor, Y. S., Richardella, A., Roushan, P., Xia, Y., Checkelsky, J. G., Yazdani, A., Hasan, M. Z., Ong,

N. P. & Cava, R. J. (2009). *Phys. Rev. B - Condens. Matter Mater. Phys.* **79**, 195208.

Hu, L., Zhu, T., Liu, X. & Zhao, X. (2014). *Adv. Funct. Mater.* **24**, 5211–5218.

Huang, F. T., Chu, M. W., Kung, H. H., Lee, W. L., Sankar, R., Liou, S. C., Wu, K. K., Kuo, Y. K. & Chou, F. C. (2012). *Phys. Rev. B - Condens. Matter Mater. Phys.* **86**, 081104.

Jia, G., Wang, X., Li, Q. & Yao, J. (2014). *Superlattices Microstruct.* **66**, 33–38.

Jiang, N. (2016). *Reports Prog. Phys.* **79**, 016501.

Klimeš, J., Bowler, D. R. & Michaelides, A. (2010). *J. Phys. Condens. Matter*. **22**, 022201.

Klimeš, J., Bowler, D. R. & Michaelides, A. (2011). *Phys. Rev. B.* **83**, 195131.

Koch, C. (2002). Determination of core structure and point defect density along dislocations.

Kolb, U., Gorelik, T., Kübel, C., Otten, M. T. & Hubert, D. (2007). *Ultramicroscopy*. **107**, 507–513.

Kresse, G. & Furthmüller, J. (1996*a*). *Comput. Mater. Sci.* **6**, 15.

Kresse, G. & Furthmüller, J. (1996*b*). *Phys. Rev. B.* **54**, 11169.

Kresse, G. & Hafner, J. (1993). *Phys. Rev. B.* **47**, 558.

Kresse, G. & Hafner, J. (1994). *Phys. Rev. B.* **49**, 14251.

Kresse, G. & Joubert, D. (1999). *Phys. Rev. B.* **59**, 1758.

Liu, B., Dong, Z. L., Hua, Y., Fu, C., Li, X., Tan, P. K. & Zhao, Y. (2018). *AIP Adv.* **8**, 115327.

Mann, C., West, D., Miotkowski, I., Chen, Y. P., Zhang, S. & Shih, C.-K. (2013). *Nat. Commun.* **4**, 2277.

March, A. (1932). *Zeitschrift Für Krist. - Cryst. Mater.* **81**, 285–297.

Meyer, J. C., Eder, F., Kurasch, S., Skakalova, V., Kotakoski, J., Park, H. J., Roth, S., Chuvilin, A., Eyhusen, S., Benner, G., Krasheninnikov, A. V. & Kaiser, U. (2012). *Phys. Rev. Lett.* **108**, 196102.

Mishra, S., Satpathy, S. & Jepsen, O. (1997). *J. Phys Condens. Matter*. **9**, 461–470.

Momma, K. & Izumi, F. (2011). *J. Appl. Crystallogr.* **44**, 1272–1276.

Nederlof, I., van Genderen, E., Li, Y.-W. & Abrahams, J. P. (2013). *Acta Crystallogr. Sect. D Biol. Crystallogr.* **69**, 1223–1230.

Palatinus, L. (2011). PETS–Program For Analysis Of Electron Diffraction Data Prague, Czech Republic: Institute of Physics of the AS CR.

Palatinus, L., Corrêa, C. A., Steciuk, G., Jacob, D., Roussel, P., Boullay, P., Klementová, M., Gemmi, M., Kopeček, J., Domeneghetti, M. C., Cámara, F. & Petříček, V. (2015). *Acta Crystallogr. Sect.*

B Struct. Sci. Cryst. Eng. Mater. **71**, 740–751.

Palatinus, L., Jacob, D., Cuvillier, P., Klementová, M., Sinkler, W. & Marks, L. D. (2013). *Acta Crystallogr. Sect. A Found. Crystallogr.* **69**, 171–188.

Palatinus, L., Petříček, V. & Corrêa, C. A. (2015). *Acta Crystallogr. Sect. A Found. Adv.* **71**, 235–244.

Perdew, J. P., Burke, K. & Ernzerhof, M. (1996). *Phys. Rev. Lett.* **77**, 3865.

Perdew, J. P., Burke, K. & Ernzerhof, M. (1997). *Phys. Rev. Lett.* **78**, 1396.

Pérez Vicente, C., Tirado, J. L., Adouby, K., Jumas, J. C., Touré, a. A. & Kra, G. (1999). *Inorg. Chem.* **38**, 2131–2135.

Petrícek, V., Dušek, M. & Palatinus, L. (2014). *Zeitschrift Fur Krist.* **229**, 345–352.

Ramachandran, V., Halfpenny, P. J. & Roberts, K. J. (2017). *Engineering Crystallography: From Molecule to Crystal to Functional Form*, Vol. edited by K.J. Roberts, R. Docherty & R. Tamura, pp. 3–19. Dordrecht: Springer Netherlands.

Roushan, P., Seo, J., Parker, C. V., Hor, Y. S., Hsieh, D., Qian, D., Richardella, A., Hasan, M. Z., Cava, R. J. & Yazdani, A. (2009). *Nature*. **460**, 1106–1109.

Sánchez-Barriga, J., Aguilera, I., Yashina, L. V., Tsukanova, D. Y., Freyse, F., Chaika, A. N., Callaert, C., Abakumov, A. M., Hadermann, J., Varykhalov, A., Rienks, E. D. L., Bihlmayer, G., Blügel, S. & Rader, O. (2018). *Phys. Rev. B.* **98**, 235110.

Scanlon, D. O., King, P. D. C., Singh, R. P., De La Torre, A., Walker, S. M., Balakrishnan, G., Baumberger, F. & Catlow, C. R. A. (2012). *Adv. Mater.* **24**, 2154–2158.

Semenkovich, S. A. & Melekh, B. T. (1972). *Chemical Bonds in Solids Volume 3: X-Ray and Thermodynamic Investigations*, Vol. pp. 159–162. Boston, MA: Springer US.

Shackelford, J. (2005). *Introduction to Material Science for Engineers*, Vol. edited by D.A. George, pp. 157–185. Pearson Education Limited.

Sheppard, D., Terrell, R. & Henkelman, G. (2008). *J. Chem. Phys.* **128**, 134106.

Simpson, R. E., Fons, P., Kolobov, A. V., Fukaya, T., Krbal, M., Yagi, T. & Tominaga, J. (2011). *Nat. Nanotechnol.* **6**, 501–505.

Sun, G., Qin, X., Li, D., Zhang, J., Ren, B., Zou, T., Xin, H., Paschen, S. B. & Yan, X. (2015). *J. Alloys Compd.* **639**, 9–14.

Tominaga, J. (2018). *MRS Bull.* **43**, 347–351.

Tominaga, J., Simpson, R. E., Fons, P. & Kolobov, A. V. (2011). *Appl. Phys. Lett.* **99**, 152105.

Tumelero, M. A., Faccio, R. & Pasa, A. A. (2016). *J. Phys. Condens. Matter*. **28**, 425801.

Unzueta, I., Zabala, N., Marín-Borrás, V., Muñoz-Sanjosé, V., García, J. A. & Plazaola, F. (2016). *Phys. Rev. B.* **94**, 43–46.

Urazhdin, S., Bilc, D., Mahanti, S. D., Tessmer, S. H., Kyratsi, T. & Kanatzidis, M. G. (2004). *Phys. Rev. B.* **69**, 085313.

Urazhdin, S., Bilc, D., Tessmer, S. H., Mahanti, S. D., Kyratsi, T. & Kanatzidis, M. G. (2002). *Phys. Rev. B.* **66**, 161306.

Van de Walle, C. G. & Neugebauer, J. (2004). *J. Appl. Phys.* **95**, 3851–3879.

Wang, L. L., Huang, M., Thimmaiah, S., Alam, A., Bud'Ko, S. L., Kaminski, A., Lograsso, T. A., Canfield, P. & Johnson, D. D. (2013). *Phys. Rev. B - Condens. Matter Mater. Phys.* **87**, 125303.

Wang, Y. L., Xu, Y., Jiang, Y. P., Liu, J. W., Chang, C. Z., Chen, M., Li, Z., Song, C. L., Wang, L. L., He, K., Chen, X., Duan, W. H., Xue, Q. K. & Ma, X. C. (2011). *Phys. Rev. B - Condens. Matter Mater. Phys.* **84**, 075335.

West, D., Sun, Y. Y., Wang, H., Bang, J. & Zhang, S. B. (2012). *Phys. Rev. B - Condens. Matter Mater. Phys.* **86**, 121201.

Wu, K. K., Ramachandran, B., Kuo, Y. K., Sankar, R. & Chou, F. C. (2016). *J. Alloys Compd.* **682**, 225–231.

Xia, Y., Qian, D., Hsieh, D., Wray, L., Pal, A., Lin, H., Bansil, A., Grauer, D., Hor, Y. S., Cava, R. J. & Hasan, M. Z. (2009). *Nat. Phys.* **5**, 398–402.

Xie, L., Yang, Z., Sun, J., Zhou, H., Chi, X., Chen, H., Li, A. X., Yao, Y. & Chen, S. (2018). *Nano-Micro Lett.* **10**, 50.

Xu, H., Chen, G., Jin, R., Pei, J., Wang, Y. & Chen, D. (2013). *CrystEngComm*. **15**, 1618–1625.

Xue, L., Zhou, P., Zhang, C. X., He, C. Y., Hao, G. L., Sun, L. Z. & Zhong, J. X. (2013). *AIP Adv.* **3**, 052105.

Yashina, L. V., Shatalova, T. B., Bobruiko, V. B., Belyansky, M. P. & Zlomanov, V. P. (1997). *Solid State Ionics*. **101**–**103**, 533–538.

Young, D. (2001). *Computational Chemistry: A Practical Guide for Applying Techniques to Real World Problems*, Vol. p. 147. John Wiley & Sons, Inc.

Zhang, H., Liu, C.-X., Qi, X.-L., Dai, X., Fang, Z. & Zhang, S.-C. (2009). *Nat. Phys.* **5**, 438–442.

Zhu, G. -z. & Botton, G. A. (2015). *Micron*. **68**, 141–145.

Zhu, T., Hu, L., Zhao, X. & He, J. (2016). *Adv. Sci.* **3**, 1600004.

Zolotoyabko, E. (2009). *J. Appl. Crystallogr.* **42**, 513–518.